Visibility Informed Covariance Analysis for Cislunar Periodic Orbits

Evangelina A. Evans
University of Colorado, Boulder

Marcus J. Holzinger
University of Colorado, Boulder

Daniel J. Scheeres
University of Colorado, Boulder

ABSTRACT

Cislunar space domain awareness (SDA) requires maintaining custody of spacecraft, which depends on both visibility and observability. This work develops a visibility-informed covariance analysis framework to evaluate how lunar phase and Earth's rotation influence the tracking of spacecraft on cislunar periodic orbits. Spacecraft dynamics are modeled using the circular restricted three-body problem, and angle-only optical observations from an equatorial ground station are simulated across a grid of initial observation epochs defined by lunar phase and time-of-day angles. The analysis computes heuristic, covariance-based metrics to quantify state uncertainty and identify favorable observation windows. Results reveal strong dependence of observability on viewing geometry, with optimal epochs aligning with specific lunar phases and local times. These findings provide actionable guidance for mission planning, highlighting how timing and orbit selection can improve state estimation accuracy, ensure flight safety, and enhance SDA capabilities in the Earth-Moon system.

1. INTRODUCTION

Cislunar space domain awareness (SDA) relies on our ability to detect and track the movement of objects in the Earth-Moon system. To maintain custody of a target and estimate its state, it must be both visible and observable. Visibility is a binary condition determined by observer constraints, such as field-of-view limitations and exclusion zones surrounding celestial bodies [7]. For ground-based observers, the visibility of cislunar objects is governed by two periods: the lunar phase cycle and Earth's daily rotation. Modeling the dynamics of a spacecraft in the rotating frame of the Earth-Moon system, these cyclic periods impose dynamic viewing constraints defined by the time-variation of angular geometries between the Sun, Earth and Moon. The epoch of an observation campaign can be mapped to an angle pairing which describes the time-of-month and time-of-day based on the relative orientations of the Sun and Earth. The collection of all angle pairings forms a month-by-day-long grid search, where each node represents a possible epoch. By iterating over a finite set of angle pairings, we can evaluate the visibility of cislunar periodic orbits across all epochs.

Visibility is a prerequisite for observability, which has traditionally been defined as a binary outcome based on the rank of the observability matrix, as described in [9]. However, recent works by [3] and [5] introduce observability metrics to quantify "how" observable an object is. In [3] a covariance-based approach integrates the information gained from a set of observation measurements over discrete time intervals to compute the information matrix, which, when inverted, produces the covariance matrix. If the information matrix is singular following an observation campaign, the object is considered unobservable.

This work provides comprehensive covariance analysis for cislunar periodic orbits across all epochs by computing heuristic, covariance-based metrics at each node in the angle-pairing grid. The epoch of an observation campaign is initialized as a node corresponding to a specific lunar phase angle and time-of-day angle. When the spacecraft is visible, collected measurements contribute to the information matrix, reducing state uncertainty. The traces of the position and velocity covariance components serve as heuristic metrics to quantify the spacecraft's state uncertainty. If the spacecraft is unobservable or if its state uncertainties exceed an acceptable threshold, that node is excluded from further analysis. As a supplementary meta-heuristic, the percentage of total observable nodes is used to assess overall observability of the orbit. At the end of the grid search, position and velocity uncertainty contours are plotted to visualize state covariance trends for the observation campaigns along the orbit as a function of initial epoch. Ideally, orbits should be observable across all nodes; however, the most favorable epochs for an observation campaign are indicated by contours of minimum state uncertainty.

This work simulates month-long observation campaigns from an equatorial ground station collecting angle-only optical measurements (azimuth and elevation) of a target placed on a periodic orbit defined by the circular restricted three-body problem (CR3BP). The orbits analyzed will include members from the Lyapunov, halo (e.g., L_2 NRHO 9:2), and axial families around the collinear Lagrange points; short and long-period orbits around the triangular Lagrange points; and distant retrograde orbits (DROs) around the Moon.

In the context of SDA, this work provides a method for assessing how the lunar phase and Earth's daily rotation cycle impact the visibility of spacecraft on cislunar periodic orbits. By systematically sampling the grid and performing covariance analysis, we can identify optimal observation windows where viewing conditions align with mission constraints, such as allowable state uncertainties. The resulting observability metrics can then inform mission planning, ensuring consistent coverage and maximizing data collection opportunities throughout the lunar cycle.

2. METHODOLOGY

In this section, we define the Circular Restricted Three-Body Problem (CR3BP) as the dynamics model used to propagate periodic orbits in the Earth-Moon system given an initial position and velocity state. We also outline a model of the earth-based equatorial ground station, for which observational measurements of the spacecraft are simulated and used to formulate a visibility-informed covariance analysis process. The mathematical notation is followed where bold lowercase letters represent vectors, bold uppercase letters represent matrices, and the superscript ^{T} notates the transpose of a matrix.

2.1 Dynamics Model: Circular Restricted Three-Body Problem

2.1.1 Equations of Motion

Spacecraft motion in the Earth-Moon system is modeled using the CR3BP. In this formulation, the spacecraft is treated as a massless particle influenced by two massive bodies, m_1 and m_2, which orbit their barycenter on circular, co-planar paths. The barycenter defines the origin of the rotating frame, which has constant angular velocity relative to an inertial frame. The x-axis points from the barycenter toward the Moon, the z-axis aligns with the system's angular momentum vector, and the y-axis completes a right-handed set.

The spacecraft state vector is defined as

$$\mathbf{x}(t) = \begin{bmatrix} \mathbf{r}(t) \\ \mathbf{v}(t) \end{bmatrix} = \begin{bmatrix} x \\ y \\ z \\ \dot{x} \\ \dot{y} \\ \dot{z} \end{bmatrix} \in \mathbb{R}^6, \tag{1}$$

where $\mathbf{r}(t) = [x\ y\ z]^T$ is the position and $\mathbf{v}(t) = [\dot{x}\ \dot{y}\ \dot{z}]^T$ is the velocity, both expressed in the CR3BP rotating frame.

The equations of motion are written as

$$\dot{\mathbf{x}}(t) = \mathbf{f}(\mathbf{x}(t), t) = \begin{bmatrix} \dot{x} \\ \dot{y} \\ \dot{z} \\ \ddot{x} \\ \ddot{y} \\ \ddot{z} \end{bmatrix}. \tag{2}$$

The acceleration terms in Eq. 2 are given by [14] as

$$\ddot{x} = x + 2\dot{y} - \frac{(1-\mu)(x+\mu)}{r_1^3} - \frac{\mu(x+\mu-1)}{r_2^3}, \tag{3}$$

$$\ddot{y} = y - 2\dot{x} - \frac{(1-\mu)y}{r_1^3} - \frac{\mu y}{r_2^3}, \tag{4}$$

$$\ddot{z} = -\frac{(1-\mu)z}{r_1^3} - \frac{\mu z}{r_2^3}, \tag{5}$$

where $\mu = \frac{m_2}{m_1+m_2} \approx 1.21505856 \times 10^{-2}$ for the Earth-Moon system, and the distances to the primaries are

$$r_1 = [(x+\mu)^2 + y^2 + z^2]^{\frac{1}{2}}, \tag{6}$$

$$r_2 = [(x-1+\mu)^2 + y^2 + z^2]^{\frac{1}{2}}. \tag{7}$$

The formulation is non-dimensionalized using the characteristic quantities:

$$\text{Distance Unit (DU):} \quad l^* = d_1 + d_2 = 384400 \text{ km}, \tag{8}$$

$$\text{Mass Unit (MU):} \quad m^* = m_1 + m_2 = 6.04582557e24 \text{ kg}, \tag{9}$$

$$\text{Time Unit (TU):} \quad t^* = \sqrt{\frac{(l^*)^3}{Gm^*}} = 3.75190262e05 \text{ seconds}. \tag{10}$$

Here, l^* is the Earth-Moon distance, m^* is the combined mass of the primaries, and t^* is derived using $G = 6.67408 \times 10^{-20}\,\text{km}^3\text{kg}^{-1}\text{s}^{-2}$. After scaling to non-dimensional (n.d.) units, the Earth-Moon distance, system mass, and angular velocity of the rotating frame are normalized to unity.

The initial state for the spacecraft is denoted by $\mathbf{x}_0 = \mathbf{x}(t_0)$. Provided $\mathbf{x}_0$, the MATLAB function `ode45` is used to numerically integrate the dynamics forward in time.

2.1.2 State Transition Matrix

The state transition matrix (STM), denoted as $\boldsymbol{\Phi}(t;t_0)$, describes the sensitivity of the spacecraft state at time t with respect to its initial state at t_0. It satisfies the linearized variational equation:

$$\dot{\boldsymbol{\Phi}}(t;t_0) = \mathbf{A}(t)\,\boldsymbol{\Phi}(t;t_0), \tag{11}$$

where $\mathbf{A}(t)$ is the system Jacobian matrix. The STM is initialized as

$$\boldsymbol{\Phi}(t_0;t_0) = \mathbf{I}_{6\times 6}, \tag{12}$$

reflecting that the state is fully sensitive to itself at the initial epoch.

The dynamics Jacobian $\mathbf{A}$ is defined as the matrix of partial derivatives of the dynamics function $\mathbf{f}(\mathbf{x}(t),t)$ with respect to the state vector $\mathbf{x}(t)$:

$$\mathbf{A}(t) = \frac{\partial \mathbf{f}}{\partial \mathbf{x}} = \begin{bmatrix} \frac{\partial \dot{\mathbf{r}}}{\partial \mathbf{r}} & \frac{\partial \dot{\mathbf{r}}}{\partial \mathbf{v}} \\ \frac{\partial \dot{\mathbf{v}}}{\partial \mathbf{r}} & \frac{\partial \dot{\mathbf{v}}}{\partial \mathbf{v}} \end{bmatrix}. \tag{13}$$

For second-order dynamics expressed in position and velocity, $\frac{\partial \dot{\mathbf{r}}}{\partial \mathbf{r}}$ is a zero block and $\frac{\partial \dot{\mathbf{r}}}{\partial \mathbf{v}}$ is the 3×3 identity matrix. The lower-left block, $\frac{\partial \dot{\mathbf{v}}}{\partial \mathbf{r}}$, contains the partial derivatives of the acceleration model with respect to position, while $\frac{\partial \dot{\mathbf{v}}}{\partial \mathbf{v}}$ accounts for any acceleration terms that depend on velocity.

Finally, the STM is numerically propagated alongside the equations of motion using the same integration scheme (e.g., MATLAB's `ode45`) to ensure consistent evolution of both the state and its linear sensitivity.

2.1.3 Lagrange Points

Five equilibrium points (libration points) exist in the CR3BP dynamical system. The collinear points, L_1–L_3, are located along the x-axis of the rotating frame, while the triangular points, L_4 and L_5, form an equilateral triangle with the Earth and Moon. The layout of the Earth–Moon system's libration points and their planar coordinates are illustrated in Figure 1.

The positions of L_4 and L_5 can be computed analytically by solving Eqs. 3–4, whereas the locations of L_1–L_3 are obtained numerically using MATLAB's `fsolve` function. The libration points' spatial locations in the CR3BP frame, along with their position coordinates, are shown in Figure 1.

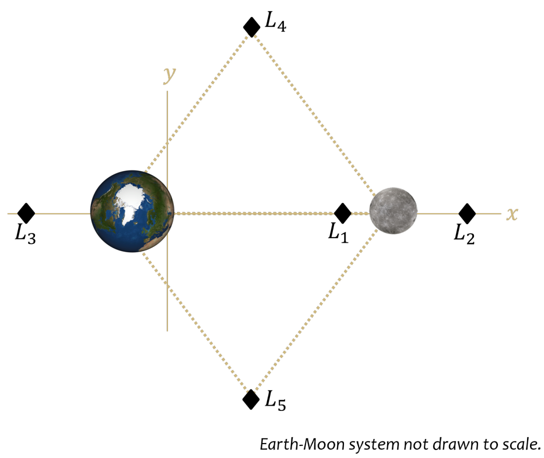

	x_{LP} (n.d.)	y_{LP} (n.d.)
L_1	0.83691513	0
L_2	1.15568217	0
L_3	-1.00506265	0
L_4	$0.5-\mu$	$\sqrt{3}/2$
L_5	$0.5-\mu$	$-\sqrt{3}/2$

Fig. 1: Earth-Moon Lagrange Points and in-plane position coordinates.

2.2 Ground Station Model

The cislunar spacecraft is tracked by an equatorial ground station located on Earth's mean radius, $R_E = 6378.137\,\text{km}$, at zero longitude ($\lambda = 0°$). For simplicity, it is assumed that Earth's equatorial plane coincides with the rotating plane of the CR3BP frame. Under this assumption, the ground station remains in-plane; however, its position relative to the CR3BP frame changes with time because Earth rotates faster than the synodic rotation of the system.

The position of the ground station expressed in the CR3BP rotating frame is given by

$$\mathbf{r}_{gs} = \mathbf{r}_E + \mathbf{r}_{gs/E} \tag{14}$$

$$= \begin{bmatrix} -\mu \\ 0 \\ 0 \end{bmatrix} + R_E \begin{bmatrix} \cos(\theta+\lambda) \\ \sin(\theta+\lambda) \\ 0 \end{bmatrix}, \tag{15}$$

where θ denotes the angle between the CR3BP x-axis and the Earth's prime meridian, and R_E has been nondimensionalized.

2.2.1 Measurements

A ground station provides azimuth (az) and elevation (el) measurements of a spacecraft relative to its local East–North–Up (ENU) frame. In this frame, the "up" direction is aligned with the radial vector from Earth's center to the ground station, the "north" direction is defined by the local angular momentum, and the "east" direction completes the right-handed coordinate system. The azimuth angle is measured clockwise from the north axis, while the elevation angle is measured upward from the local east–north plane tangent to Earth's surface.

The unit vectors defining this ENU frame are given by [8]:

$$\hat{\mathbf{E}} = \frac{\hat{\mathbf{Z}} \times \hat{\mathbf{U}}}{\|\hat{\mathbf{Z}} \times \hat{\mathbf{U}}\|}, \quad \hat{\mathbf{N}} = \hat{\mathbf{U}} \times \hat{\mathbf{E}}, \quad \hat{\mathbf{U}} = \frac{\mathbf{r}_{gs/E}}{\|\mathbf{r}_{gs/E}\|}, \tag{16}$$

where $\hat{\mathbf{Z}} = \begin{bmatrix} 0 & 0 & 1 \end{bmatrix}^T$ is the $+z$ axis of the CR3BP frame (normal to the rotating plane). The resulting unit vectors are expressed in the same coordinate system as the relative position vector $\mathbf{r}_{gs/E}$.

To simulate measurements, the range vector is first computed as

$$\boldsymbol{\rho} = \mathbf{r} - \mathbf{r}_{gs}, \tag{17}$$

where $\mathbf{r}$ and $\mathbf{r}_{gs}$ denote the spacecraft and ground station positions, respectively. This Cartesian vector is then transformed from the CR3BP frame to the local ENU frame via a rotation matrix:

$$\boldsymbol{\rho}^{ENU} = \mathbf{R}_{3BP}^{ENU}\, \boldsymbol{\rho}^{3BP}, \tag{18}$$

where the rotation matrix is defined as

$$\mathbf{R}_{3BP}^{ENU} = \begin{bmatrix} \hat{\mathbf{E}}^T \\ \hat{\mathbf{N}}^T \\ \hat{\mathbf{U}}^T \end{bmatrix}, \tag{19}$$

after evaluating Eq. 16 using relative position and velocity vectors expressed in the CR3BP frame.

Finally, measurements are generated by mapping $\boldsymbol{\rho}^{ENU}$ to azimuth and elevation angles [8, 1]:

$$az = \operatorname{atan2}\left(\frac{\rho_E}{\rho_N}\right), \tag{20}$$

$$el = \operatorname{asin}\left(\frac{\rho_U}{\rho}\right), \tag{21}$$

where $\rho = \|\boldsymbol{\rho}\|$ is the magnitude of the range and ρ_i denotes the corresponding ENU component.

Measurement uncertainty arises from various sources, including instrument calibration and performance, atmospheric effects, pointing error, and data processing. This uncertainty is modeled using the measurement noise covariance matrix:

$$\mathbf{R} = \begin{bmatrix} \sigma_{az}^2 & 0 \\ 0 & \sigma_{el}^2 \end{bmatrix}, \tag{22}$$

where $\sigma_{az} = \sigma_{el} = 10$ arcseconds represents a typical value reflecting the general capabilities of ground-based observatories and telescopes [2, 13, 16].

2.2.2 Visibility Constraints

For a ground station to collect observational measurements, the target must be visible, which means that its geometric position relative to the station satisfies a set of viewing constraints. Table 1 summarizes the constraints implemented for an Earth-based observer. A target is considered visible only if all constraints are satisfied.

Table 1: Viewing constraints for an Earth-based observer.

Constraint	Value	Type	Definition
Astronomical Twilight	12°	Horizon angle	Observations are conducted at night, when the geometric center of the Sun is below the horizon [12]
Elevation Mask	10°	Horizon angle	Minimum elevation angle above the horizon for target tracking, accounting for local interference [11]
Lunar Exclusion	10°	Cone half-angle	Target is occluded when aligned with the Moon; angle measured relative to the line-of-sight (LOS) to the Moon's geometric center [6]
Solar Exclusion	30°	Cone half-angle	Target is occluded when aligned with the Sun; angle measured relative to the LOS to the Sun's geometric center [6]

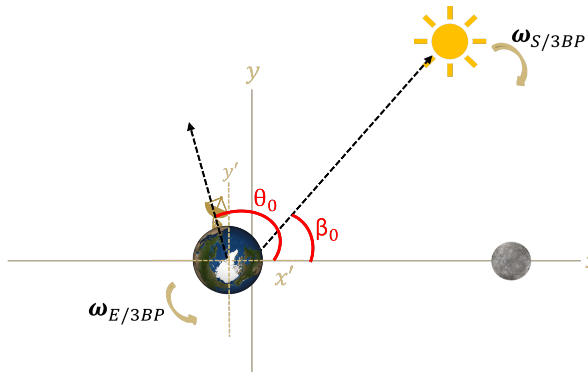

Fig. 2: θ_0 and β_0 angle definitions in the CR3BP frame.

2.3 Initial Epoch: Change of Time Coordinate Representation

Each viewing constraint depends on the instantaneous geometric orientation of the observer relative to the Earth, Sun, Moon, and spacecraft. Over the course of cislunar periodic orbit, these orientations change according to the lunar phase cycle and Earth's sidereal rotation.

An orbit's initial epoch can be mapped to an initial angle pair, (θ_0, β_0), representing the Earth's rotation angle and the Sun's angular position in the CR3BP frame, respectively — referred to as the "time-of-day" and "lunar phase" angles. As shown in Fig. 2, θ_0 measures Earth's rotation relative to the CR3BP frame, while β_0 specifies the Sun's angular position in the rotating Earth-Moon plane. While epochs defined by a Julian date and time are unique, the angular geometries of the celestial bodies in the CR3BP repeat synodically. Consequently, all Julian-date initial epochs correspond to a finite set of angles: $\theta_0 \in [0°, 360°]$ and $\beta_0 \in [0°, 360°]$.

By transforming the time coordinate system to define an initial epoch based on planetary geometric alignment, one obtains a dynamic but repeatable time coordinate, (θ_0, β_0), that captures the relevant observational geometry.

Starting from an initial rotation angle θ_0, the Earth-fixed longitude of the ground station in the rotating frame evolves as

$$\theta(t) = \theta_0 + t\ \omega_{E/3BP}, \tag{23}$$

with the relative rotation rate defined as

$$\omega_{E/3BP} = \omega_E + \omega_{3BP}, \tag{24}$$

where ω_E is Earth's sidereal spin rate (T = 23:56:04.09 hours/t^* TU), ω_{3BP} is the inertial angular velocity of the CR3BP rotating frame ($T = 2\pi$ TU), and the period T is related to angular velocity by $\omega = 360°/T$. Similarly, the lunar-phase angle moves clock-wise in the CR3BP frame following

$$\beta(t) = \beta_0 + t\ \omega_{S/3BP}, \tag{25}$$

with the relative rotation rate defined as

$$\omega_{S/3BP} = \omega_S - \omega_{3BP}, \tag{26}$$

where ω_S is the sidereal period of the Earth-Sun system (31,558,149.8 seconds/t^* TU).

2.4 Visibility-Informed Covariance Analysis

Orbit determination uses observational measurements to estimate the spacecraft state. The accuracy of these measurements directly affects the quality of the resulting state estimate. For a given orbit, one can predict the expected information gain by simulating the collection of measurements at discrete time steps along the trajectory. The methodology presented here follows the approach developed in [4].

2.4.1 Information Gain

The information gain, $\mathbf{\Lambda}$, is accumulated over consecutive observations using the measurement update in a batch-processing framework [15]. The measurement vector is defined as

$$\mathbf{G} = \begin{bmatrix} az \\ el \end{bmatrix}, \tag{27}$$

with the corresponding measurement Jacobian

$$\tilde{\mathbf{H}}_i = \frac{\partial \mathbf{G}}{\partial \mathbf{x}} = \frac{\partial \mathbf{G}}{\partial \boldsymbol{\rho}} \frac{\partial \boldsymbol{\rho}}{\partial \mathbf{x}} = \begin{bmatrix} \frac{\rho_N}{\rho_e^2+\rho_N^2} & -\frac{\rho_E}{\rho_e^2+\rho_N^2} & 0 \\ -\frac{\rho_E \rho_N}{\rho_h \rho^2} & -\frac{\rho_N \rho_U}{\rho_h \rho^2} & \frac{\rho_h}{\rho_h \rho^2} \end{bmatrix} \mathbf{R}_{3BP}^{ENU} \tag{28}$$

where $\rho_h = \sqrt{\rho_E^2 + \rho_N^2}$. Note that $\tilde{\mathbf{H}}_i$ becomes undefined when the spacecraft passes directly through zenith such that $\rho_N = \rho_E = 0$; measurements are omitted on these rare occurrences. The matrix $\tilde{\mathbf{H}}_i$ maps the state sensitivity (of the CR3BP dynamics system) to sensitivities in the measurement space as:

$$\mathbf{H}_i = \tilde{\mathbf{H}}_i \mathbf{\Phi}(t_i; t_0). \tag{29}$$

The information gain matrix is updated incrementally as

$$\mathbf{\Lambda} \leftarrow \mathbf{\Lambda} + \mathbf{H}_i^T \mathbf{R}^{-1} \mathbf{H}_i, \tag{30}$$

where $\mathbf{\Lambda}$ is initialized as zero at t_0 and accumulates during the observation campaign as measurements are collected.

2.4.2 Covariance

The covariance matrix is related to the information gain as its inverse:

$$\mathbf{P} = \mathbf{\Lambda}^{-1}. \tag{31}$$

At the end of an observation campaign, the spacecraft is considered unobservable if the information matrix is singular and thus non-invertible. (Note: the term "observable" in this context does not correspond to the linear control definition of observability, which depends on the rank of the observability matrix.)

The position and velocity components of $\mathbf{P}$ can be partitioned into submatrices:

$$\mathbf{P} = \begin{bmatrix} \mathbf{P}_{rr} & \mathbf{P}_{rv} \\ \mathbf{P}_{vr} & \mathbf{P}_{vv} \end{bmatrix}, \tag{32}$$

where the diagonal submatrices $\mathbf{P}_{rr}$ and $\mathbf{P}_{vv}$ represent the position and velocity covariances, respectively, and the off-diagonal submatrices represent the cross-covariances between position and velocity.

The overall position and velocity uncertainties are defined as

$$\sigma_r = \sqrt{\mathrm{tr}(\mathbf{P}_{rr})}, \tag{33}$$

$$\sigma_v = \sqrt{\mathrm{tr}(\mathbf{P}_{vv})}. \tag{34}$$

For cases where $\mathbf{\Lambda}$ is invertible but yields excessively large uncertainties, upper limits are imposed:

$$\tilde{\sigma}_r = 1000\,\mathrm{km}, \tag{35}$$

$$\tilde{\sigma}_v = 0.01\,\mathrm{km/s}. \tag{36}$$

If either σ_r or σ_v exceeds its respective threshold, the orbit initialized at that epoch is considered unobservable, effectively eliminating epoch nodes that cannot reasonably be tracked within acceptable uncertainty limits.

2.4.3 Heuristic Metrics

To systematically compare the observability of different orbits, we define metrics that capture how observability varies across all possible epochs. The following covariance-based heuristic metrics are used:

- **Metric #1:** The smallest position and velocity uncertainty across all nodes. Smaller values indicate better tracking accuracy at the observable nodes.
- **Metric #2:** The largest position and velocity uncertainty among observable nodes. When the uncertainty exceeds the maximum allowable threshold at any node, this metric reflects the highest uncertainty observed for the remaining observable epochs, representing a worst-case scenario.
- **Metric #3:** The fraction of epochs that are observable. A higher fraction offers more flexibility for selecting a transfer epoch and reduces the risk of missing viable observation windows due to delays.

3. IMPLEMENTATION

This study considers representative members from several periodic orbit (PO) families in the CR3BP; the initial conditions of which are provided in Table 2, obtained from the National Aeronautics and Space Administration (NASA) Jet Propulsion Laboratory (JPL) Three-Body Periodic Orbit Catalog [10]. The procedure for implementing the described visibility-informed covariance analysis on these POs is as follows:

Step 1: Select a trajectory. Initialize the trajectory state with $\mathbf{x}_0$ of the desired CR3BP PO found in Table 2.

Step 2: Define the grid search. The grid search is parameterized by the finite set of geometry-based time coordinates, $\theta_0 \in \{0:10:360°\}$ and $\beta_0 \in \{0:10:360°\}$, the unique angle pairings correspond to an initial epoch of the trajectory.

Step 3: Simulate the observation campaign. For each node (θ_0, β_0) in the grid search, initialize the geometric orientation of the Sun and ground station within the CR3BP. Propagate the orbit for 2π TU, a full rotation of the Earth–Moon system. During propagation, visibility constraints relative to the ground station are evaluated in hourly time steps, and measurements are collected whenever the spacecraft is visible.

The simulation assumes that all measurements satisfying the visibility constraints in Section 2.2.2 are collected, although in practice operational constraints (e.g., maximum telescope slew rates, illumination, etc.) may prevent this.

Step 4: Compute the information gain & covariance. Using the simulated azimuth and elevation measurements collected at each time step, the information gain is updated according to Eq. 30. Performing this update for all collected measurements yields the hypothetical total information gained throughout the observation campaign, and in turn, estimates the state uncertainty, σ_r and σ_v, of the spacecraft traveling along the PO for each node.

Step 5: Quantify observability of the trajectory across all initial epochs. After iterating over all nodes in the grid search, contours of σ_r and σ_v are plotted as a function of the initial-epoch angle-pairings. Analysis of these plots indicates which epochs provide the best observability of the orbit. The three heuristic metrics introduced in Section 2.4 are then computed to characterize the orbit by: 1) the range of uncertainty seen across all epochs and 2) the percentage of initial epochs for which the spacecraft can be successfully observed.

Table 2: Periodic orbits in the CR3BP selected for covariance analysis.

Orbit	State Vector, $\mathbf{x}_0$ (n.d.)	Jacobi Constant, C	Period, T (n.d.)
Lunar DRO	$\begin{bmatrix} 6.8355909882592514E-1 \\ 1.9414482129110789E-23 \\ -4.7191016718963267E-25 \\ -1.6753163837408492E-13 \\ 7.2752642654283473E-1 \\ 1.1511771211953919E-26 \end{bmatrix}$	$2.85765E+0$	$5.02986E+0$

Continued on next page

Table 2 – *Continued from previous page*

Orbit	State Vector, $\mathbf{x}_0$ (n.d.)	Jacobi Constant, C	Period, T (n.d.)
L_1 Lyapunov	$\begin{bmatrix} 7.98302899167086E-01 \\ 3.24991084576810E-28 \\ -2.04745216007438E-33 \\ -1.06343142101902E-14 \\ 3.68336489836938E-01 \\ -9.23775401130423E-32 \end{bmatrix}$	$2.56597E+0$	$3.38367E+0$
L_2 NRHO 9:2	$\begin{bmatrix} [1.021783951720710 \\ 1.719168552737911e-13 \\ -0.181947613459008 \\ 2.326182672406602e-13 \\ -0.102748024688004 \\ -9.371644251241410e-13] \end{bmatrix}$	$1.98015E+0$	$1.50798E+0$
L_3 Axial	$\begin{bmatrix} -1.0056658526069755E+0 \\ 9.4851992227284655E-24 \\ 1.5245959814533124E-12 \\ 5.7714075093723999E-13 \\ 1.4926996612649710E+0 \\ 8.6788098705711170E-1 \end{bmatrix}$	$3.07783E-2$	$6.26660E+0$
L_4 Short-Period	$\begin{bmatrix} 4.8784941344943100E-1 \\ 1.4712659587392278E+0 \\ -7.1668479976413883E-33 \\ 1.0248413867893715E+0 \\ -7.8822421924800468E-1 \\ 1.1705177779386463E-31 \end{bmatrix}$	$2.01810E+0$	$6.28583E+0$
L_4 Long-Period	$\begin{bmatrix} 4.8784941344943100E-1 \\ 6.7212754533055685E-1 \\ 1.7393275630338904E-35 \\ -0.245350313518527 \\ 1.3805858489246356E-1 \\ -3.03577844584586E-35 \end{bmatrix}$	$2.99796E+0$	$2.40714E+1$

4. RESULTS

Section 4 presents the observability analysis of the CR3BP POs listed in Table 2, evaluated using the visibility-informed covariance framework described in Sections 2.4 and 3. The analysis is performed as a two-dimensional grid search over initial observation epochs, parameterized by the time-of-day angle θ_0 and lunar-phase angle β_0. For each PO, contour maps of the total position and velocity standard deviations, σ_r and σ_v, computed from all measurements collected over the month-long observation campaign, are generated as functions of (θ_0, β_0) in Figs. 3-7, with the corresponding minimum and maximum values summarized in Table 3.

These contours characterize the sensitivity of state estimation performance to observational geometry, highlighting regions in the (θ_0, β_0) domain where uncertainty growth is minimized. Blue-shaded regions correspond to favorable epochs yielding low state uncertainty and strong observability, whereas yellow regions indicate degraded performance with high uncertainty. White-filled nodes denote epochs at which the spacecraft is unobservable due to insufficient measurement geometry or lack of visibility. To quantify overall observability across the month-long campaign, the percentage of observable nodes is also reported for each orbit. This metric provides a comparative measure of the robustness of different POs to visibility-driven constraints and informs trajectory selection and scheduling strategies for space domain awareness operations.

Table 3: Range of minimum and maximum position and velocity uncertainties across all epochs and percentage of observable epochs for the cislunar periodic orbits.

Orbit	Min σ_r, km	Max σ_r, km	Min σ_v, km/s	Max σ_v, km/s	Observable Epochs
Lunar DRO	5.83688	54.16370	$1.17050E-5$	$5.16547E-5$	100%
L_1 Lyapunov	30.68283	999.10979	$1.96599E-4$	$5.42916E-3$	94.38%
L_2 NRHO 9:2	9.427312	314.06480	$1.12988E-4$	$1.10008E-3$	100%
L_3 Axial	2.60430	41.63761	$1.01873E-5$	$1.55977E-4$	100%
L_4 Short-Period	5.12248	54.60939	$1.24251E-5$	$1.90333E-3$	100%
L_4 Long-Period	5.20825	19.43071	$1.18027E-5$	$2.91755E-5$	100%

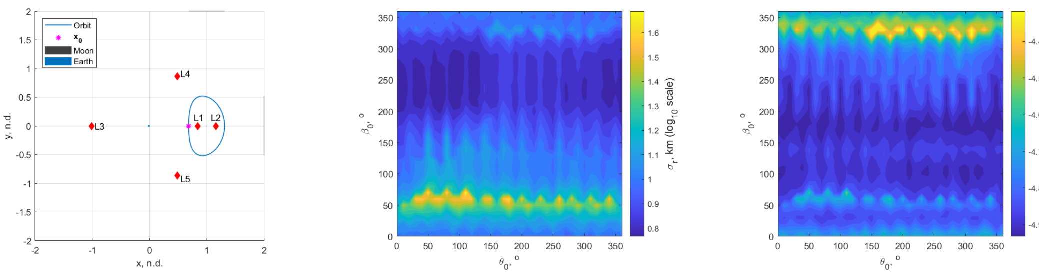

Fig. 3: Lunar DRO, observation campaign duration $= 2\pi$ TU.

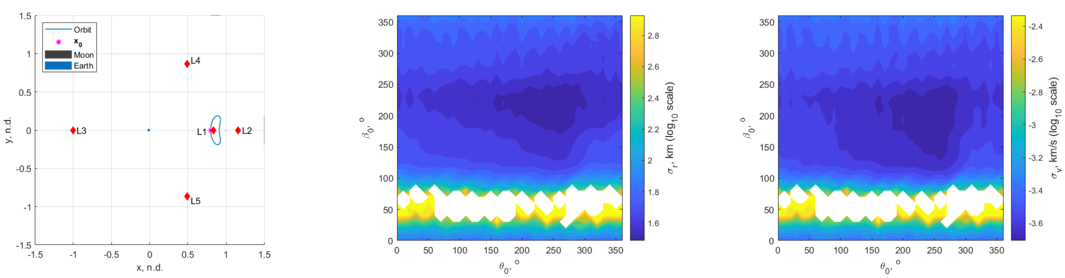

Fig. 4: L_1 Lyapunov orbit, observation campaign duration $= 2\pi$ TU.

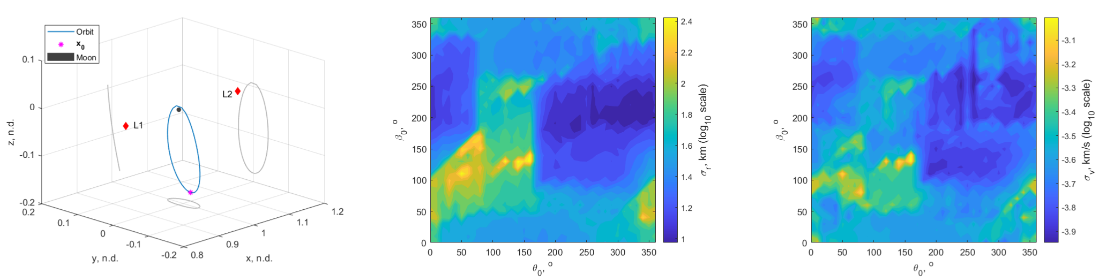

Fig. 5: L_2 NRHO, observation campaign duration $= 2\pi$ TU.

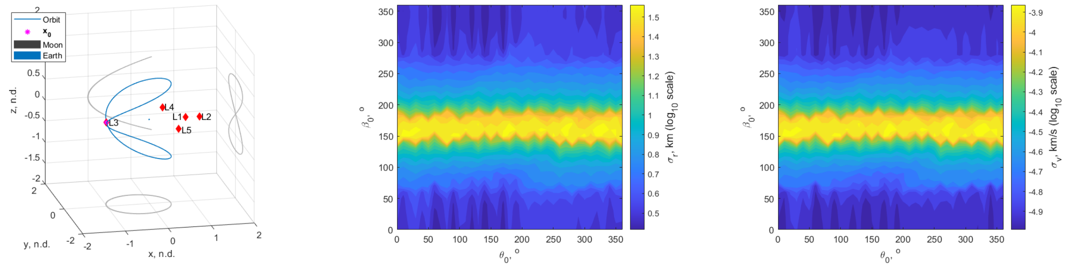

Fig. 6: L_3 axial orbit, observation campaign duration $= 2\pi$ TU.

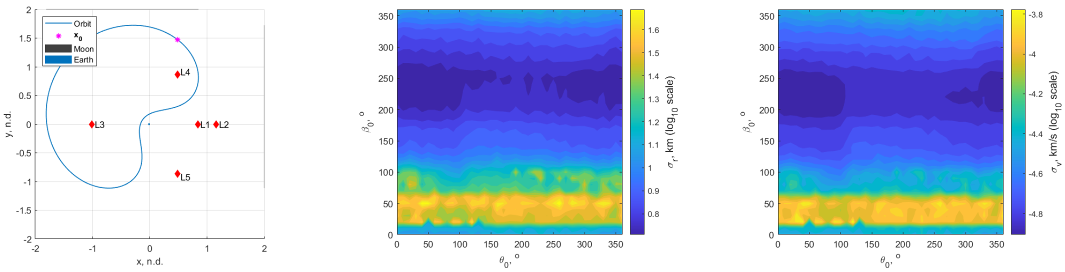

Fig. 7: L_4 short-period orbit, observation campaign duration $= 2\pi$ TU.

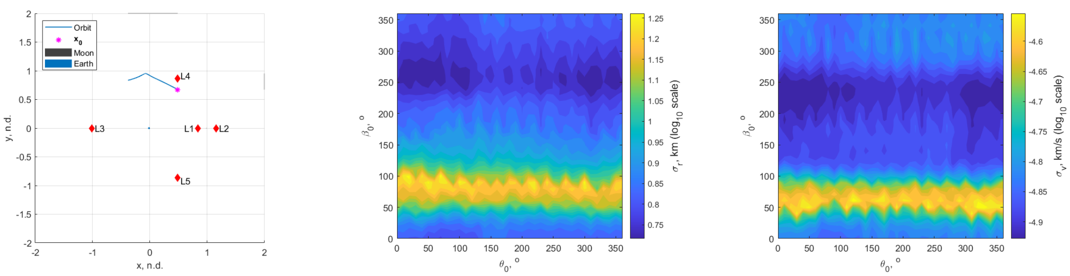

Fig. 8: L_4 long-period orbit, observation campaign duration $= 2\pi$ TU.

5. DISCUSSION

5.1 Key Observations from Visibility-Informed Covariance Analysis

Observation 1: *Observability of cislunar POs is primarily constrained by the solar exclusion zone, which introduces extended periods of invisibility regardless of local time geometry.*

The contour maps for each PO, with the exception of Fig. 5, reveal a dominant horizontal band of high state uncertainty across the (θ_0, β_0) grid. This feature corresponds to the solar exclusion constraint, which prohibits observations when the spacecraft lies within a certain angular separation from the Sun. Because this constraint is tied to the Sun–Earth–observer geometry, its impact manifests as a function of lunar phase rather than local time, producing the horizontal structure in the uncertainty contours. During these intervals, the lack of measurements degrades the information matrix, resulting in elevated σ_r and σ_v values or rendering the spacecraft unobservable. Consequently, this band represents an epoch range during which observation campaigns are least effective, regardless of the time-of-day angle.

In Fig. 6, a strong horizontal band appears for $\beta_0 \approx 140°$–$190°$, where the Sun is aligned with the Earth–spacecraft line-of-sight (LOS) during the initial portion of the campaign. Missing these early observations is particularly detrimental because initial measurements strongly constrain the propagated uncertainty over the remainder of the campaign. Without them, the state estimate evolves from a poorly informed prior, and later measurements cannot fully recover the lost information. In contrast, if early measurements are available and visibility gaps occur later, the propagated uncertainty remains lower because the initial state is better estimated. This explains why solar exclusion at the start of the campaign typically produces higher-uncertainty bands in the visibility-informed covariance analysis.

> **Observation 2:** *Observability for lunar-vicinity orbits is primarily dictated by orbit size and geometry: smaller-radius trajectories remain within the lunar exclusion zone, while larger-radius orbits provide sufficient clearance to maintain visibility and enable tracking.*

A secondary limitation arises for orbits in close proximity to the Moon, such as certain DROs and halo or Lyapunov orbits about L_1 and L_2. Members of these orbit families can maintain small radial distances from the lunar surface, causing them to remain entirely—or for the majority of the observation campaign—within the lunar exclusion zone. In such cases, no observable nodes are recorded because the spacecraft is never visible to the ground station. This result underscores an important mission design consideration: orbit size and geometry in the lunar vicinity must be carefully engineered to avoid persistent lunar occlusion and ensure adequate visibility for tracking. Neglecting this constraint can lead to trajectories that are effectively unobservable, compromising state estimation performance and the ability to maintain custody.

To mitigate this, the lunar-vicinity orbits listed in Table 3 have been chosen with sufficiently large radii to remain mostly outside the lunar exclusion zone, enabling simulated measurements to support visibility-informed covariance analysis. For example, the DRO and L_1 Lyapunov orbits shown in Figs. 3 and 4 illustrate how orbit size impacts observability. Comparison of the two indicates that the smaller-radius L_1 Lyapunov orbit exhibits initial epochs that are completely unobservable, whereas the larger-radius DRO can be tracked across all epochs. For the smaller L_1 Lyapunov orbit, only the upper and lower edges of the "bean"-shaped trajectory extend beyond the lunar exclusion zone, providing intermittent visibility. However, if the initial β_0 angle places the Sun behind the upper edge at the start of the campaign, its apparent motion (progressing clockwise in the CR3BP rotating frame) will subsequently obscure the lower edge, resulting in zero visibility throughout the month. This geometric progression explains why the corresponding β_0 band of unobservability is shifted to approximately 30°–80° in Fig. 4.

> **Observation 3a:** *Contours of σ_r and σ_v identify subsets of initial epochs that minimize state uncertainty, providing optimal windows for initiating observation campaigns.*

Favorable initial epochs correspond to regions in the (θ_0, β_0) domain where both σ_r and σ_v are minimized, typically located outside the solar exclusion band. Overlaying these contours identifies finite subsets of initial epochs that jointly minimize overall state uncertainty. Initiating the orbit during one of these campaign windows is critical to achieving the lowest estimation error. From a mission planning perspective, these subsets are particularly valuable because each (θ_0, β_0) orientation maps to multiple Julian dates, giving planners flexibility in selecting departure opportunities while still ensuring robust tracking performance.

> **Observation 3b:** *The percentage of observable epochs provides a complementary measure of orbit robustness. A higher percentage indicates that the orbit offers broader opportunities for successful observation, making it less sensitive to precise scheduling and operational delays*

Unlike the localized minima highlighted by σ contours, this metric captures how consistently an orbit remains observable across the entire (θ_0, β_0) grid. High coverage reflects reduced sensitivity to precise epoch selection and greater resilience to scheduling uncertainties or operational delays. Orbits with 100% coverage may not always achieve minimal state uncertainties—as shown for the L_2 NRHO in Table 3—but they ensure acceptable tracking across a wide range of epochs, which is particularly valuable for long-duration missions where fixed departure dates cannot be guaranteed.

5.2 Extending Visibility-Informed Covariance Analysis to Higher-Dimensional PO Parameter Spaces

All trajectories in the CR3BP preserve their spatial geometry regardless of the selected initial epoch; however, the viewing geometry — which is critical for evaluating visibility-informed covariance analysis — does vary with epoch. In [4], the visibility-informed covariance analysis methodology is applied to cislunar transfer trajectories from Earth-Moon Lagrange points to geosynchronous Earth orbit (GEO). These transfers were defined by fixed departure and arrival states, which bounded the trajectory and determined a finite time-of-flight (TOF) during which the spacecraft traveled along the transfer path. Observation campaigns could only be simulated while the spacecraft remained in-flight along the transfer trajectory. Once the spacecraft reached GEO, the transfer was complete, and the observation campaign concluded.

In contrast, the CR3BP POs considered in this work are closed trajectories where the spacecraft returns to its initial state after a fixed orbital period. A PO can be initialized at any point along the orbit, and as the state propagates forward in time, observation campaigns can span any fraction or multiple of the orbital period. This introduces two additional degrees of freedom to the visibility-informed covariance analysis when applied to cislunar POs: the initial state along the orbit and the campaign duration. To standardize the evaluation across selected POs, this study restricts the solution space to variation in the initial epoch only. The additional degrees of freedom were parameterized by fixing the initial state and limiting campaign durations to 2π TU. This duration aligns with the Earth-Moon synodic period and one complete rotation of the Sun relative to the CR3BP rotating frame. Consequently, short-period orbits may complete multiple revolutions within this time, whereas long-period orbits complete only a partial revolution (see Fig. 8).

This section serves as an initial investigation into the influence of observation campaign duration and initial state selection on overall observability. A full exploration of the higher-dimensional solution space, including comprehensive grid searches and result formulation, is reserved for future work.

5.2.1 Effect of Observation Campaign Duration on Observability Results

The impact of observation campaign duration on observability results depends strongly on the orbital period and spatial extent of the trajectory. To illustrate this effect, we consider two representative cases: the L_2 NRHO with $T < 2\pi$ TU (where $4T \approx 2\pi$ TU) and the L_4 long-period orbit with $T \gg 2\pi$ TU. Each case is evaluated for observation campaigns of 2π, T, and $3T$ duration.

> **Observation 4:** *The spatial extent of an orbit dictates the range of relative geometries that can be assessed for visibility constraints during an observation campaign. Larger orbits span broader regions of cislunar space, requiring longer campaigns to capture a complete set of viewing geometries, whereas smaller orbits remain confined to limited spatial regions and exhibit a restricted range of line-of-sight configurations.*

The L_2 NRHO occupies a relatively small spatial region, causing the LOS vector in the Earth–Moon frame to sweep a limited angular range. This results in less geometric diversity when evaluating visibility constraints. Contours generated for varied campaign durations in Figs.9–11 show that regions of favorable initial epochs remain largely unchanged when the campaign duration is a multiple of the orbital period. Additionally, the percentage of initial epochs that maintain trackability increases as the observation duration grows. This occurs because extending the campaign over integer multiples of T, and approximately 2π, causes the viewing geometry to repeat, recollecting measurements at similar orientations. This behavior aligns with the expectation that longer campaigns, improve observability by sampling recurring geometries—as reflected by the decreasing values of σ_r and σ_v in Table 4 with increased campaign duration.

> **Observation 5:** *Observation campaigns that span integer multiples of both the orbit period and the the CR3BP frame rotation period more consistently evaluate analogous relative geometries, reducing variability in observability results.*

In contrast, the L_4 long-period orbit spans a much larger region, and a fixed campaign duration of 2π TU is insufficient for the spacecraft to traverse the entire orbit. Consequently, visibility constraints are evaluated for only a fractional subset of possible angular geometries between the ground station, Sun, Moon, and spacecraft. Orbits covering large spatial regions introduce greater diversity in LOS orientations, requiring longer campaigns to achieve comprehensive coverage and improved observability metrics. This produces variation in observability contours favorable initial epoch regions as the campaign duration changes. For example, the primary horizontal solar-occlusion band in Figs. 12–14 is vertically shifted depending on the duration of the observation campaign. This effect underscores the importance of scaling campaign length appropriately for orbits with greater spatial extent.

Table 4: Range of minimum and maximum position and velocity uncertainties across all epochs and percentage of observable epochs for the L_2 NRHO, compared by observation campaign duration.

Orbit	Campaign Duration, TU	Min σ_r, km	Max σ_r, km	Min σ_v, km/s	Max σ_v, km/s	Observable Epochs
L_2 NRHO 9:2	2π	9.427312	314.06480	$1.12988E-4$	$1.10008E-3$	100%
	T	222.39977	525.26584	$2.27754E-4$	$9.89581E-3$	26.73%
	$3T$	14.62016	838.75417	$1.23504E-4$	$8.49070E-3$	86.12%

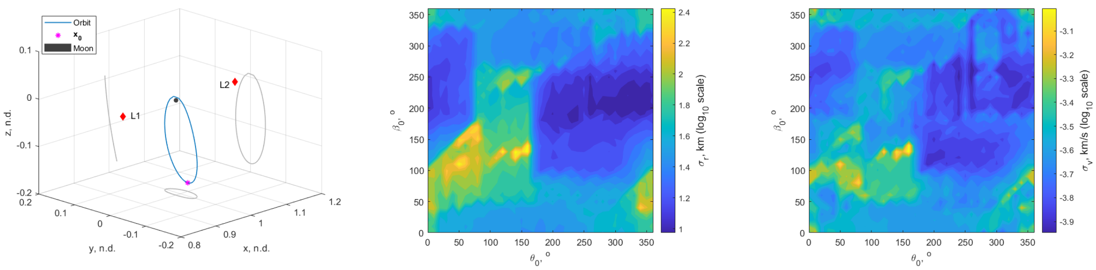

Fig. 9: L_2 NRHO, observation campaign duration $=2\pi$ TU ($\approx 4T$).

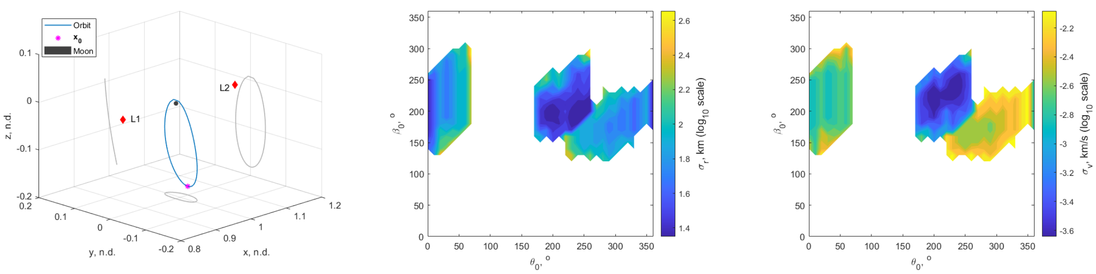

Fig. 10: L_2 NRHO, observation campaign duration $= T$.

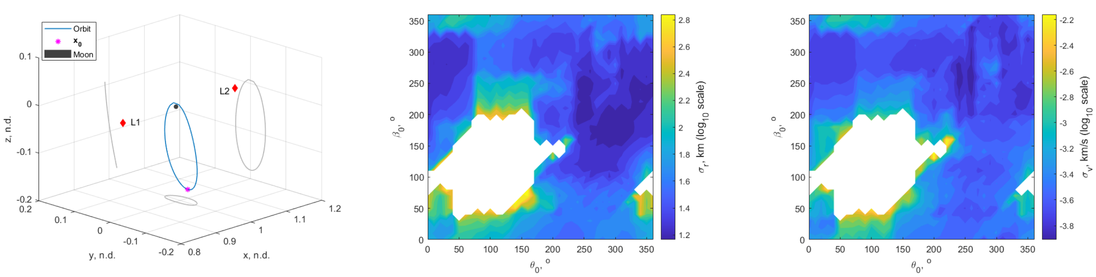

Fig. 11: L_2 NRHO, observation campaign duration $= 3T$.

In summary, observation campaigns yield more consistent results when (1) the orbit remains confined to a smaller spatial region, and (2) the campaign duration is an integer multiple of the orbit period rather than a fraction. Longer campaigns become particularly important for large, long-period orbits to capture the full range of viewing geometries necessary for robust observability.

Table 5: Range of minimum and maximum position and velocity uncertainties across all epochs and percentage of observable epochs for the L_4 long-period orbit, compared by observation campaign duration.

Orbit	Campaign Duration, TU	Min σ_r, km	Max σ_r, km	Min σ_v, km/s	Max σ_v, km/s	Observable Epochs
L_4 Long Period	2π	5.20825	19.43071	$1.18027E-5$	$2.91755E-5$	100%
	T	5.11122	54.60939	$1.23945E-5$	$1.90333E-4$	100%
	$3T$	2.01945	6.57152	$5.29921E-6$	$1.55702E-5$	100%

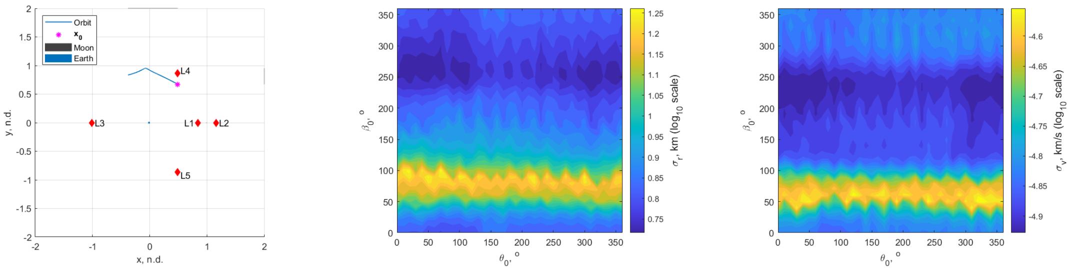

Fig. 12: L_4 long-period orbit, observation campaign duration $= 2\pi$ TU ($\approx \frac{1}{4}T$).

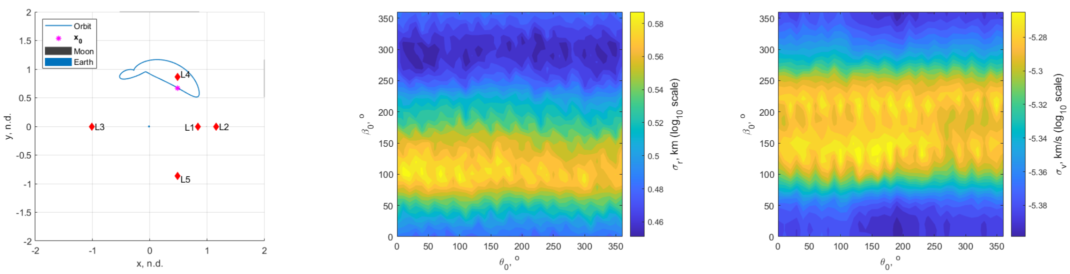

Fig. 13: L_4 long-period orbit, observation campaign duration $= T$.

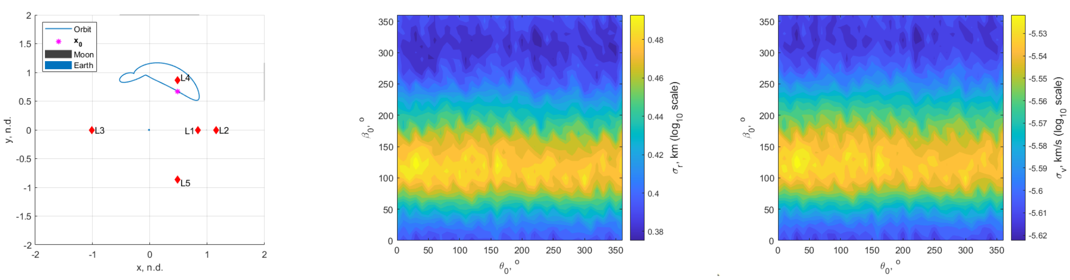

Fig. 14: L_4 long-period orbit, observation campaign duration $= 3T$.

5.2.2 Effect of PO Initial State on Observability Results

An initial state uniquely determines a trajectory in the CR3BP. However, a PO can be initialized from any point along its closed path, as the endpoint of the trajectory will coincide with the initial state from which it was propagated. Choosing different initial states along the orbit effectively shifts the spacecraft's viewing geometry, which in turn influences the observability outcomes based on the chosen $\mathbf{x}_0$.

Observation 6: *The observability of the spacecraft as it travels along the orbit depends on the selected initial epoch.*

To illustrate this effect, we examine the L_4 short-period orbit over an observation campaign lasting 2π time units (TU). In Figs. 15–18, we phase the spacecraft's initial state along the orbit by increments of $\frac{1}{4}T$. This phasing results in a vertical shift of the solar-occlusion-induced low-observability band in the contour maps.

Table 6: Range of minimum and maximum position and velocity uncertainties across all epochs and percentage of observable epochs for the L_4 short-period orbit, compared by varying initial state along the orbit.

Orbit	$\mathbf{x_0}$	Min σ_r, km	Max σ_r, km	Min σ_v, km/s	Max σ_v, km/s	Observable Epochs
L_4 Short Period	$\mathbf{x_{t_0}}$	5.12248	54.60939	$1.24251E-5$	$1.90333E-3$	100%
	$\mathbf{x_{t_0+\frac{1}{4}T}}$	1.87180	373.76425	$4.85713E-5$	$8.87516E-3$	99.20%
	$\mathbf{x_{t_0+\frac{1}{2}T}}$	12.07274	405.16174	$3.44645E-5$	$8.96683E-4$	100%
	$\mathbf{x_{t_0+\frac{3}{4}T}}$	10.71409	142.42325	$2.82599E-5$	$3.78914E-4$	100%

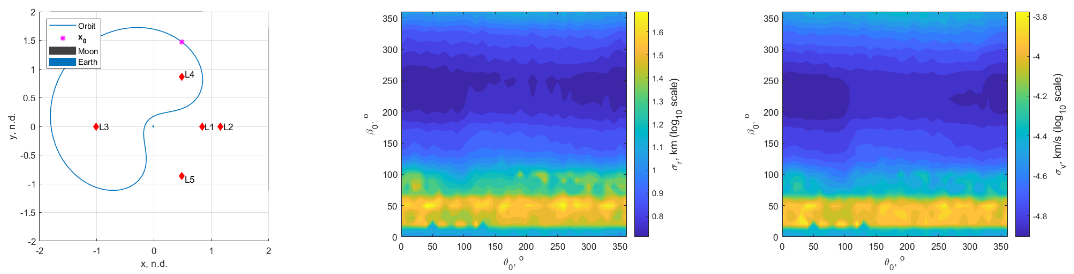

Fig. 15: L_4 short-period orbit, observation campaign duration $= 2\pi$ TU ($\approx T$).

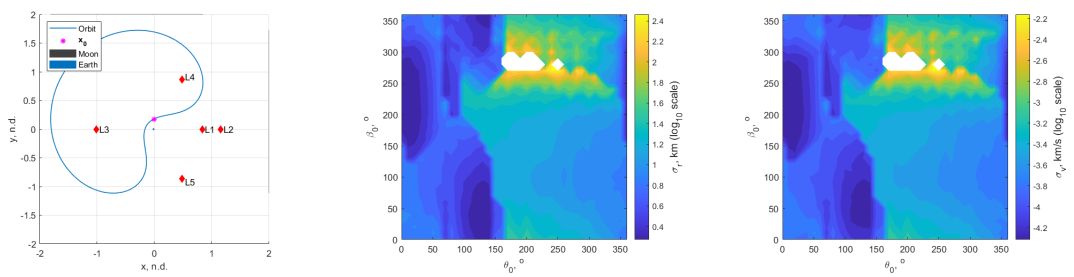

Fig. 16: L_4 short-period orbit, observation campaign duration $= 2\pi$ TU, $\mathbf{x_0}$ cycled to $t_0 + T/4$.

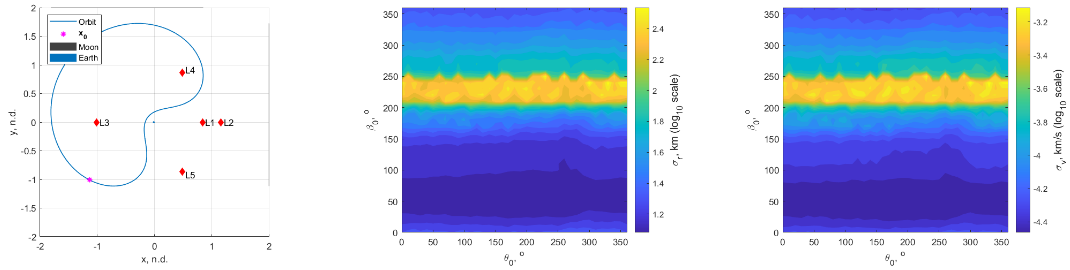

Fig. 17: L_4 short-period orbit, observation campaign duration $= 2\pi$ TU, $\mathbf{x_0}$ cycled to $t_0 + T/2$.

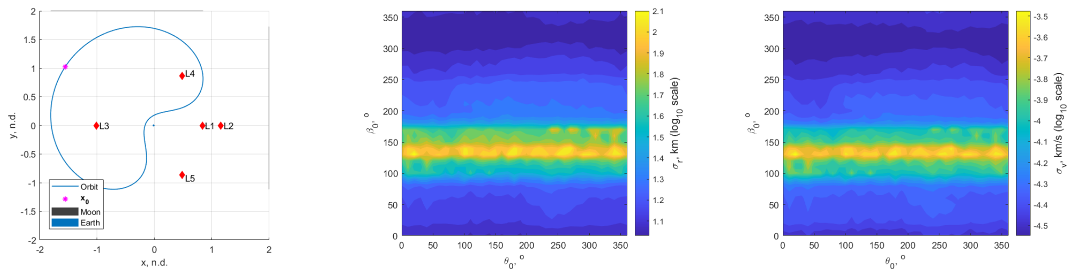

Fig. 18: L_4 short-period orbit, observation campaign duration $= 2\pi$ TU, $\mathbf{x_0}$ cycled to $t_0 + 3T/4$.

When designing missions, there are two key strategies to address the selection of an initial state along the orbit and the corresponding initial epoch:

1. Identify a suitable initial epoch for all possible initial states along the trajectory. Introduce the initial state as a third dimension in the grid search and perform the visibility-informed covariance analysis. Then stack or overlay the contour maps of σ_r and σ_v for all initial conditions, similar to a heatmap. Overlapping low-uncertainty regions across all contours will identify initial epochs that are collectively favorable for any initial state along the orbit.

2. Given a specific orbit injection point, determine the optimal injection epoch. Depending on the transfer design method, the resulting trajectory may specify a particular injection point along the desired PO destination. Once this point is identified, a visibility-informed covariance analysis can be performed to select an injection epoch that ensures sufficient observation opportunities while the spacecraft remains on the PO. From this injection epoch, the required departure epoch from the spacecraft's origin location can then be determined.

Selecting an optimal initial epoch is crucial for maintaining spacecraft custody, ensuring space situational awareness, and supporting overall mission safety.

6. CONCLUSION

This work developed a visibility-informed covariance analysis framework to quantify how lunar phase, Earth's rotation, and orbit geometry shape the observability of spacecraft on cislunar periodic orbits. By systematically mapping initial observation epochs through a two-dimensional grid of lunar phase and local time, the study revealed strong dependencies between viewing geometry and state uncertainty. Results show that solar exclusion dominates periods of unobservability, lunar-vicinity orbits require careful design to avoid persistent occlusion, and optimal epochs can be identified where both position and velocity uncertainties are minimized.

While this study fixed the initial state along each periodic orbit and limited observation campaigns to 2π TU, future work should explore the broader parameter space defined by variable initial states, longer campaign durations, and higher-dimensional orbit families. Additional extensions include incorporating operational constraints, modeling space-based sensor architectures, and evaluating multi-station ground networks to capture a more realistic picture of cislunar tracking. Expanding in these directions will further strengthen the utility of visibility-informed covariance analysis for mission design and SDA planning.

Overall, these findings provide actionable guidance for mission planning and space domain awareness operations in the Earth–Moon system. By integrating visibility-informed covariance metrics into trajectory selection and observation scheduling, operators can reduce state uncertainty, maintain spacecraft custody, and improve the safety and resilience of future cislunar missions.

7. ACKNOWLEDGMENT

This work was funded by the Space University Research Initiative (SURI) program (FA9550-23-1-0726), sponsored by the Air Force Office of Scientific Research (AFOSR) and the Air Force Research Laboratory (AFRL) Chief Technologist Office. The views expressed are those of the authors and do not reflect the official guidance or position of the United States Government, the Department of Defense, or of the United States Air Force.

REFERENCES

[1] Joshua Block, David Curtis, Robert Bettinger, and Adam Wilmer. Cislunar sda with low-fidelity sensors and observer uncertainty. 09 2022.

[2] Massimo Capaccioli and Pietro Schipani. The vlt survey telescope opens to the sky: history of a commissioning. *The Messenger*, 146:2–7, 2011.

[3] Andrew D. Dianetti, Ryan M. Weisman, and John L. Crassidis. Application of observability analysis to space object tracking. In *AIAA Guidance, Navigation, and Control Conference*, 2017.

[4] Evangelina A. Evans, Marcus J. Holzinger, and Daneil J. Scheeres. Visibility informed covariance analysis for cislundar transfer trajectories. In *2025 AAS/AIAA Astrodynamics Specialist Conference*, 2025.

[5] E. E. Fowler and D. A. Paley. Observability metrics for space-based cislunar domain awareness. *The Journal of Astronautical Scienes*, 70(11), 2023.

[6] Maaninee Gupta and Kathleen C Howell. Cislunar trajectory design for constellations leveraging sidereal-synodic resonant behavior. In *2024 AAS/AIAA Astrodynamics Specialist Conference*, 2024.

[7] M. Klonowski, Casey Heidrich, Naomi Owens-Fahrner, and Marcus J. Holzinger. Analysis of persistent detection corridors for cislunar space situational awareness. In *Advanced Maui Optical and Space Surveillance Technologies Conference*, 2024.

[8] Darin Koblick and Joseph Choi. Cislunar orbit determination benefits of moon-based sensors. 09 2022.

[9] Justin Kruger and Simone D'Amico. Observability analysis and optimization for angles-only navigation of distributed space systems. *Advances in Space Research*, 73(11):5464–5483, 2024.

[10] NASA Jet Propulsion Laboratory. Three-body periodic orbit catalog, 2025. Accessed: 2025-08-24.

[11] National Geodetic Survey. User guidelines for single base real time gnss positioning. https://www.ngs.noaa.gov/PUBS$_LIB/NGSRealTimeUserGuidelines.v2.0.pdf$,2009.

[12] National Weather Service. Types of twilight. https://www.weather.gov/lmk/twilight-types, 2023. Accessed: 2025-07-20.

[13] NOIRLab Engineering Team. Ctio blanco 4-m telescope pointing model and performance, 2020.

[14] Bruce A. Prussing, John E. Conway. Orbital mechanics, second edition. pages 65–66. Oxford University Press, 2013.

[15] Byron D. Tapley, Bob E. Schutz, and George H. Born. Statistical orbit determination. pages 194–199. Academic Press, Burlington, 2004.

[16] Telescope and Site Subsystem Team. Pointing test plan and performance goals. Technical Report LTS-206, Vera C. Rubin Observatory, 2019.